Electrodeposition of preferentially oriented zinc for flow-assisted alkaline batteries

CrossMark

Divyaraj Desai [a], Xia Wei [a], Daniel A. Steingart [b,c], Sanjoy Banerjee [a,*]

[a] CUNY Energy Institute & Department of Chemical Engineering, City College of New York, New York, NY, USA
[b] Department of Mechanical and Aerospace Engineering, Princeton University, Princeton, NJ, USA
[c] Andlinger Center for Energy and the Environment, Princeton University, Princeton, NJ, USA

HIGHLIGHTS

- Compact zinc deposited on brass is shown to have ~60% $11\bar{2}2$ preferred orientation.
- Preferentially oriented zinc has a coulombic efficiency of 99% over 100 cycles.
- Texture is observed in the orientation with the lowest nucleation work function.
- Highest preferred texture is observed at the minimum in the total cell resistance.

ARTICLE INFO

ABSTRACT

Preferred orientation of zinc deposits during charging is shown to significantly improve performance and cycle life in flow-assisted alkaline zinc batteries, which has not been demonstrated earlier. The preferred orientation of zinc deposits was investigated using X-ray diffraction (XRD). Compact zinc is found to have $(11\bar{2}2)$ preferred orientation on brass, which contributes to ~60% of the texture. The effect of charging current and zincate concentration on morphology was investigated in a rotating hull cell and correlated with anodic efficiency. Compact zinc deposits are found to have a fine-grained, bright finish and the highest anodic efficiency. Electrochemical impedance spectroscopy (EIS) proves that compact zinc corresponds to the minimum in the half-cell resistance. Morphological control using compact zinc could be accomplished using innovations such as pulse charging or enhanced mass-transfer to improve anode performance without affecting the cathode.

1. Introduction

The demand for grid-scale energy storage has necessitated the development of batteries with high energy and power densities. Alkaline zinc-anode batteries offer a low-cost, scalable solution to meet this requirement. However, zinc redistribution on periodic cycling and dendrite formation is known to severely limit battery life to 200 cycles [1]. Growth of mass-transfer limited zinc dendrites leading to an internal short circuit is the primary failure mode of these batteries. In recent years, flow-assisted Zn–NiOOH batteries have been developed to circumvent this limitation and offer a significant improvement in cycle life up to 1000–1500 cycles [2,3].

Preferred orientation in electrodeposited metals was first reported by Pangarov [4], and nanocrystalline zinc with preferred orientation is reported to offer superior protection on galvanized steels [5]. The development of texture on alkaline zinc deposits and the effect on morphology has not been previously explored. Textured zinc electrodes, with their lower corrosion rates and fewer grain boundaries offer a potential improvement in flow-assisted zinc batteries. The effect of operating conditions of choice of substrate, current density and concentration on texture have not been explored, and it is desirable to be able to determine *a priori* the conditions in which preferred orientation is highest. Due to the complex kinetics of zinc deposition and dissolution, there is considerable discrepancy in the literature values for exchange current density (i_0) and Tafel slopes [6–8]. The timescales of the ohmic, kinetic and mass-transport processes have been reported and explained by EIS models [9,10]. However, these models address either the kinetically limited formation of mossy zinc or the mass-

transfer limited formation of zinc dendrites but cannot do both simultaneously.

The morphologies of zinc have been previously reported as mossy, compact and dendritic [8,11,12], and have been correlated to the ratio of applied to limiting current density (i/i_{lim}), or the CD-ratio [13]. Mossy zinc deposited at $i/i_{lim} <0.2$ is porous, adheres poorly to the current collector and eventually fails by the loss of electrical contact. This loss of active material is the cause of progressive loss of battery capacity. Mossy zinc has a larger specific surface area, so the nominal corrosion/self-discharge currents are proportionately higher. Hydrogen evolution occurs at low current densities due to zinc corrosion by equation (1):

$$Zn + 2H_2O \rightleftharpoons Zn(OH)_2 + H_2 \qquad (1)$$

Compact zinc is reported to deposit at $i/i_{lim} >0.2$ and is reported to have a dense structure that is conformal with the current collector [14]. Relatively low surface area and compact profile are desirable to ensure low self-corrosion rates and prevent the initiation of dendritic growth [15–17] to have highly efficient long-cycling anodes with negligible capacity degradation. By comparison, dendritic zinc is deposited at $i/i_{lim} >1$ and is accompanied by vigorous hydrogen evolution. Inefficient zinc deposition coupled with the increased likelihood of battery failure through an internal short circuit makes dendritic zinc particularly undesirable. Morphological control in battery electrodes, specifically compact zinc deposition, has not been effectively explored. The lack of research interest probably stems from the older batteries operating in a stagnant electrolyte. The stringent mass-transport led to mossy zinc deposits being the morphology of choice, since their larger surface area reduced the effective current density. The advent of flow-assisted batteries has made it possible to explore faster charging protocols and morphology control to improve the performance and cycle life of zinc anodes.

The purpose of this study is to investigate the performance of compact zinc deposits with preferred orientation in concentrated alkaline electrolyte. X-ray diffraction (XRD) is used to investigate the effect of current density ratio (i/i_{lim}) on phase composition and the development of preferred orientation. The degree of texture is quantified from the XRD peaks using the method of Berube and L'Esperance [18] and reported as a relative texture coefficient (RTC). Rotating cylinder Hull (RCH) cell [19] experiments were performed to parameterize the effect of zincate concentration and current density on morphology and determine the transition between mossy, compact and dendritic zinc. Scanning electron microscopy (SEM) is used to determine the microstructure of zinc deposits. The regime of compact zinc formation is determined and optimized to improve electrode performance. Electrochemical impedance spectroscopy (EIS) is used to deduce the timescales of the microscopic processes in zinc deposition, and the current density ratio for minimum impedance is determined. The optimal operating conditions also correspond to the maximum preferred orientation. Galvanostatic half-cell cycling experiments are performed to compare the improvement in performance of preferentially-oriented zinc.

2. Experimental

2.1. Materials

All the experiments were performed using zinc oxide (ZnO) dissolved in 45 wt% potassium hydroxide (11.6 mol L^{-1}) as the electrolyte purchased from Sigma–Aldrich (ACS grade). Unless specified explicitly, the ZnO concentration was 60 g L^{-1} (0.74 mol L^{-1}). The electrolyte was freshly prepared by dissolving a mixture of zinc oxide and potassium hydroxide at 60 °C before experiments were conducted. De-aeration was not performed and experimental conditions sufficiently mimic battery operation. The reference electrode was Hg/HgO in 20 wt% KOH (Koslow Industries).

2.2. Rotating cylindrical hull cell setup

The primary current distribution varies predictably across the length of a cylindrical Hull cell electrode in a control, which means that the effect of current density on morphology can be analyzed in a single experiment. A rotating cylinder Hull cell (HT Autolab) was used to investigate the dependence of zinc morphology on current density. The working electrode was a cylindrical brass rod 0.6 cm diameter, and 8 cm long. The zincate concentration in the electrolyte was varied (0.38–1.24 mol L^{-1}) to validate that the transition between different zinc morphologies is independent of zincate concentration. The rotation speed was varied in a manner such that i/i_{lim} varied in the same regime across all the experiments. The average thickness of zinc deposited (50 C cm^{-2}) was kept constant across all the experiments. The samples were titrated with acetic acid using bromothymol blue as indicator to a neutral pH (6.0–7.6), rinsed multiple times with DI water, rinsed with acetone, and vacuum dried at room temperature. This sample preparation step helped minimize ex-situ oxidation of the electrode.

2.3. X-ray diffraction setup

X-ray diffraction (XRD) was used to investigate the material composition and preferred orientation of the zinc morphologies. All flat-plate experiments were performed with the flow-assisted prismatic cell described in our previous work [13]. A 3.5×1.8 cm brass sheet (Orbel Industries) was used as anode with a 3.5×1.8 cm sintered nickel cathode (Jiangsu Highstar Battery Manufacturing). The nominal thickness of the electrodeposited zinc was 25 μm across all the experiments, at which the zinc would be impervious to X-rays. X-ray diffraction (XRD) experiments were carried out in a Philips Panalytical XRD operating at 40 kV/40 mA with a Cu-Kα filter. Pole figures were generated using a Bruker D8 diffractometer, and inverse pole figures were generated using the MTEX algorithm [20].

2.4. Electrochemical impedance spectroscopy (EIS) setup

EIS half-cell experiments were performed using the frequency response mode on the Versastat 4 (Princeton Applied Research) to investigate the timescales of the processes in zinc deposition. A 0.5 cm copper rotating disk electrode (Pine Instruments) was used as the anode and a single 3.5×1.8 cm sintered nickel sheet was the cathode. The reference electrode was paralleled with a platinum wire using a 0.05 μF capacitor to eliminate stray impedances associated with the reference electrode at frequencies in excess of 10 kHz [21].

3. Results and discussion

3.1. Morphologies of zinc deposition

A rotating cylindrical Hull (RCH) cell was used to investigate the effect of local current density on the morphologies of zinc deposition. The benefit of using an RCH cell is that the local current density varies as a function of electrode position, making it possible to investigate morphological transitions in a range of current densities in a single experiment.

The primary current distribution along an RCH cell varies along the length of the electrode and is given by equation (2) [22]:

$$\frac{i(z)}{i_{avg}} = \frac{0.535 - 0.458z}{(0.0233 + z^2)^{1/2}} + 8.52*10^{-5} \exp(7.17z) \qquad (2)$$

where z is the dimensionless distance along the length of the anode, $i(z)$ is the local current density, and i_{avg} is the nominal current density.

The limiting current (i_{lim}) is given by equation (3):

$$i_{lim} = 0.0791nFC_{Zn}U^{0.7}d^{-0.3}\nu^{-0.344}D_{Zn}^{0.644} \qquad (3)$$

where C_{Zn} and D_{Zn} are the zincate concentration and diffusivity, U is the rotational velocity, d is the electrode diameter, and ν is the kinematic viscosity. The rotation speed was adjusted so that the limiting current density was equal to half the average current density. The average charge passed was 50 C cm^{-2} across all the experiments. The concentrations of zinc oxide that were chosen were 40, 60, 80 and 100 g L^{-1} of ZnO.

Fig. 1 shows the morphology of zinc deposited on a typical RCH electrode viewed under an optical microscope. The zinc deposited at a low current density ratio on the electrode is dark grey, porous and patchy. At a higher current density a transition to shiny light grey zinc is observed, which deposits as a compact and adherent layer. At current densities close to the limiting current, zinc deposits as a dark grey, coarse-grained layer.

The deposition morphology changes significantly as a function of the applied current density, summarized in Fig. 2. The area fraction of shiny zinc was calculated by analyzing the optical microscopy images using ImageJ software. The deposit can be characterized based on the ratio of applied to limiting current densities (i/i_{lim}). It is clear that dark grey, friable zinc deposits are formed at $i/i_{lim} < 0.3$. This feature appears to be independent of the zincate concentration in the electrolyte, and the area fraction of compact zinc collapses on a single curve. Compact, bright zinc is formed when $0.3 < i/i_{lim} < 1$, and transitions to coarse-grained dark grey zinc at current densities excess of the limiting current. The compact area fraction drops beyond the limiting current, and almost no compact zinc is observed at current densities excess of 1.5i_{lim}.

Scanning electron microscopy (SEM) images reveal the microstructure of the zinc morphologies (Fig. 3). Mossy zinc is comprised of a large number of zinc fibers ($\sim$1 micron thick) growing in random directions. A thin film is observed on some of the deposits and is thought to be a blocking layer of ZnO. The poor strength of mossy zinc is attributed to its relatively high porosity. At higher resolution, two kinds of pores are observed. Small pores ($\sim$1 μm) formed by interweaving zinc fibers and larger pores ($\sim$10 μm) are
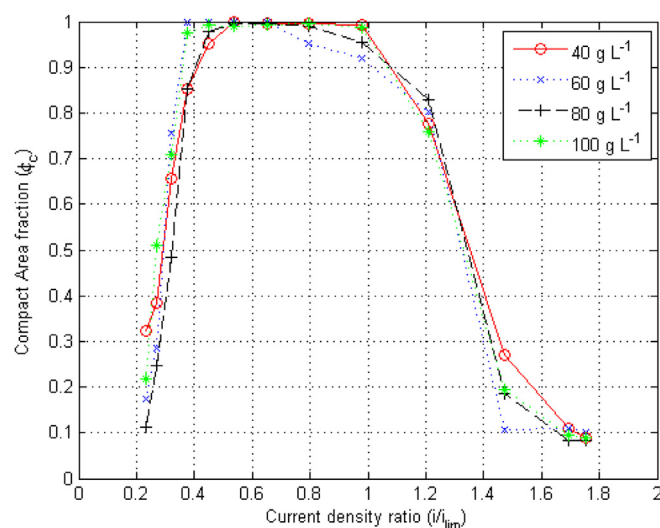

Fig. 2. Plot of areal fraction of compact zinc versus the current density ratio.

probably formed by hydrogen evolution as a result of zinc corrosion. There is no discernable preferred growth direction. By comparison, the shiny zinc deposits comprise stacks of hexagonal zinc crystallites due to the 6-fold anisotropy of zinc growth. The crystal grains are typically 5–10 μm in size, and are compactly packed. The low surface area also implies that corrosion/self-discharge rates on such compact deposits are expected to be significantly lower than mossy zinc. The formation of zinc dendrites occurs due to the instability of a growing interface under mass-transfer limited growth. At conditions in excess of the mass-transfer limiting current density, leaf-like zinc deposits were observed. Secondary branches are observed as the zinc crystallites increase the surface area in order to stabilize the interface, in accordance with the linear instability of an interface under galvanostatic electrodeposition [16]. The size of the dendritic deposits was typically 50–100 μm. The formation of such deposits frequently leads to battery failure through an internal short circuit [23].

3.2. Preferred orientation of zinc deposits

X-ray diffraction was used as a tool to confirm the presence of the ZnO layer and determine the presence of preferred orientation in zinc deposits. Weak reflections of $(10\bar{1}0)$ and $(00\bar{0}2)$ ZnO were detected at $i/i_{lim} = 0.1$ and $i/i_{lim} = 0.2$, but are completely absent for $i/i_{lim} > 0.4$ and are attributed to a ZnO layer that vanishes with

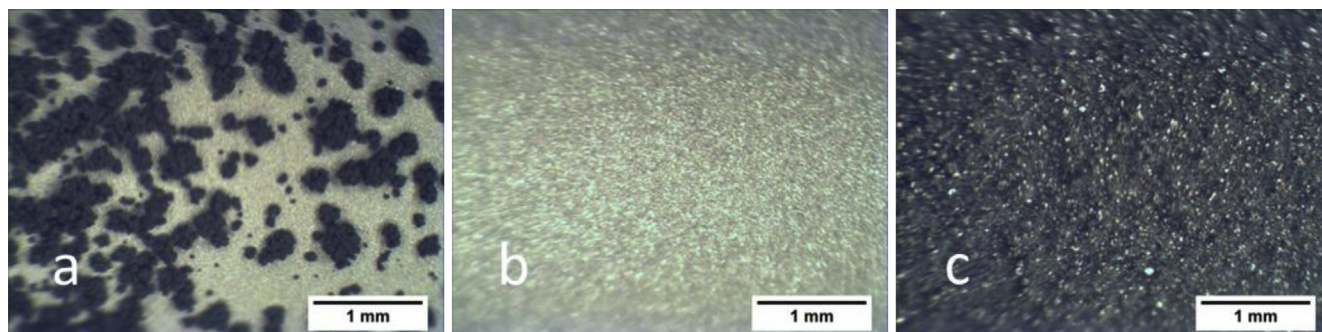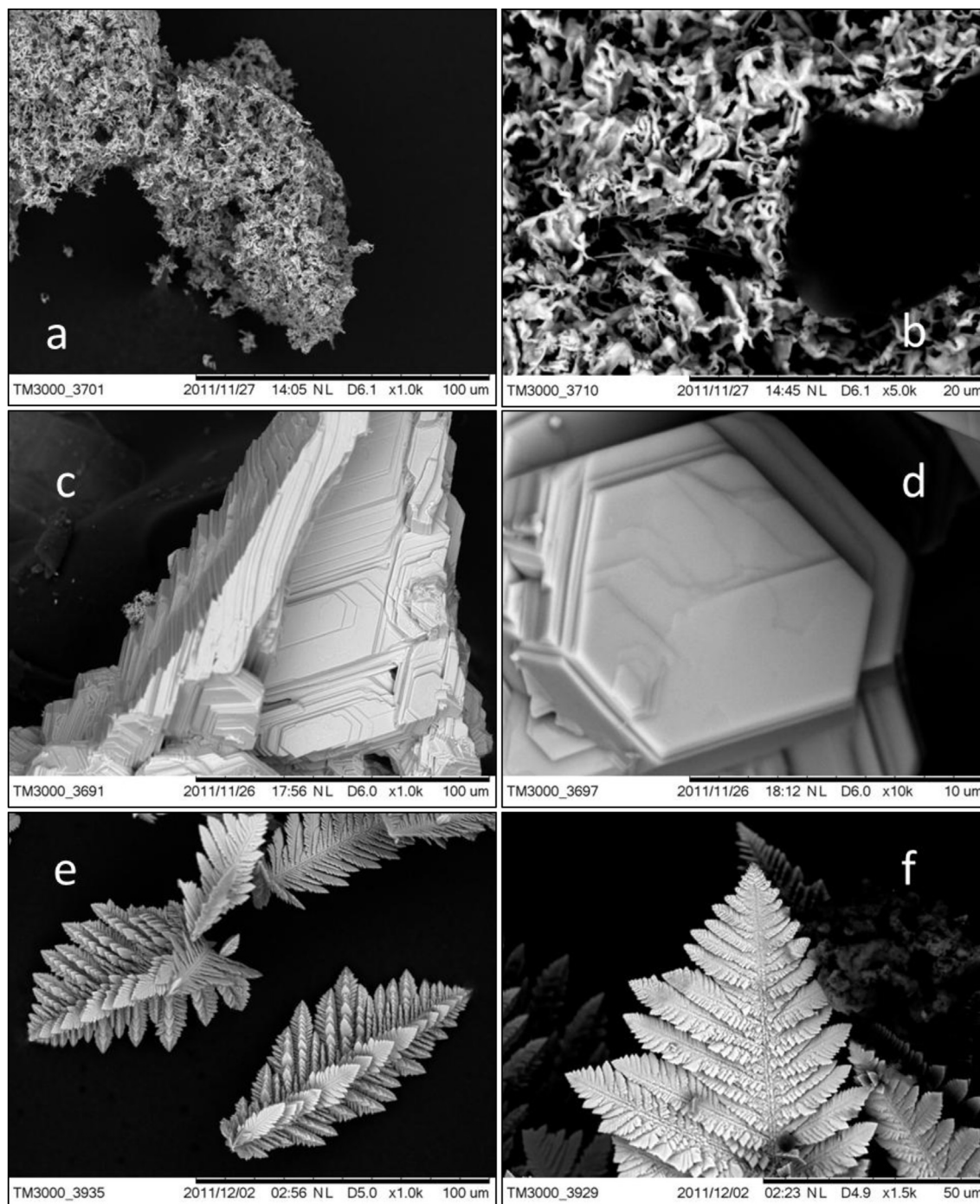**Fig. 1.** Zinc deposited on an RCH cell at 60 g L^{-1} ZnO. The macroscopic morphology changes from scattered mossy to compact and finally to coarse. The local current density for the images was (a) 10 (b) 25 and (c) 40 mA cm^{-2}. The limiting current density was $i_{lim} = -40$ mA cm^{-2}.

Fig. 3. Morphology of zinc deposits is (a and b) mossy at $i/i_{lim} = 0.13$, (c and d) compact at $i/i_{lim} = 0.67$ and (e and f) dendritic at $i/i_{lim} = 1.2$.

increasing overpotential (Fig. 4a). The prominent Zn peaks observed were $(10\bar{1}0)$, $(000\bar{2})$, $(11\bar{2}0)$, $(10\bar{1}1)$, and $(11\bar{2}2)$.

The XRD patterns were analyzed to understand the role of preferred orientation in zinc deposition. The extent of preferred orientation is clear from the inverse pole figures. Preferred orientation $(11\bar{2}2)$ is observed at $i/i_{lim} = 0.6$, indicating fiber texture is present in compact deposits, but neither mossy nor dendritic deposits have distinguishable texture. The texture of the prominent zinc reflections is quantified (Fig. 4b) by comparing with the diffraction pattern of an amorphous zinc powder following the procedure reported by Berube and L'Esperance [18]. The preferred

orientation was reported in terms of a texture coefficient (TC) and a relative texture coefficient (RTC) which is interpreted as the % composition of a given orientation. A value of TC > 1 indicates preferred orientation is present in the sample. The computed texture coefficients and compositions of each orientation are reported in Table 1. At low current density ratios ($i/i_{lim} = 0.05$ and $i/i_{lim} = 0.1$) the diffraction pattern closely resembles that of a fine powder, and no texture is observed. Preferred orientation in the $(11\bar{2}2)$ direction is strongest in $0.5 \leq i/i_{lim} \leq 0.8$, with ~60% of zinc depositing in the $(11\bar{2}2)$ orientation. More than one preferred orientation is observed to dominate at higher current densities,
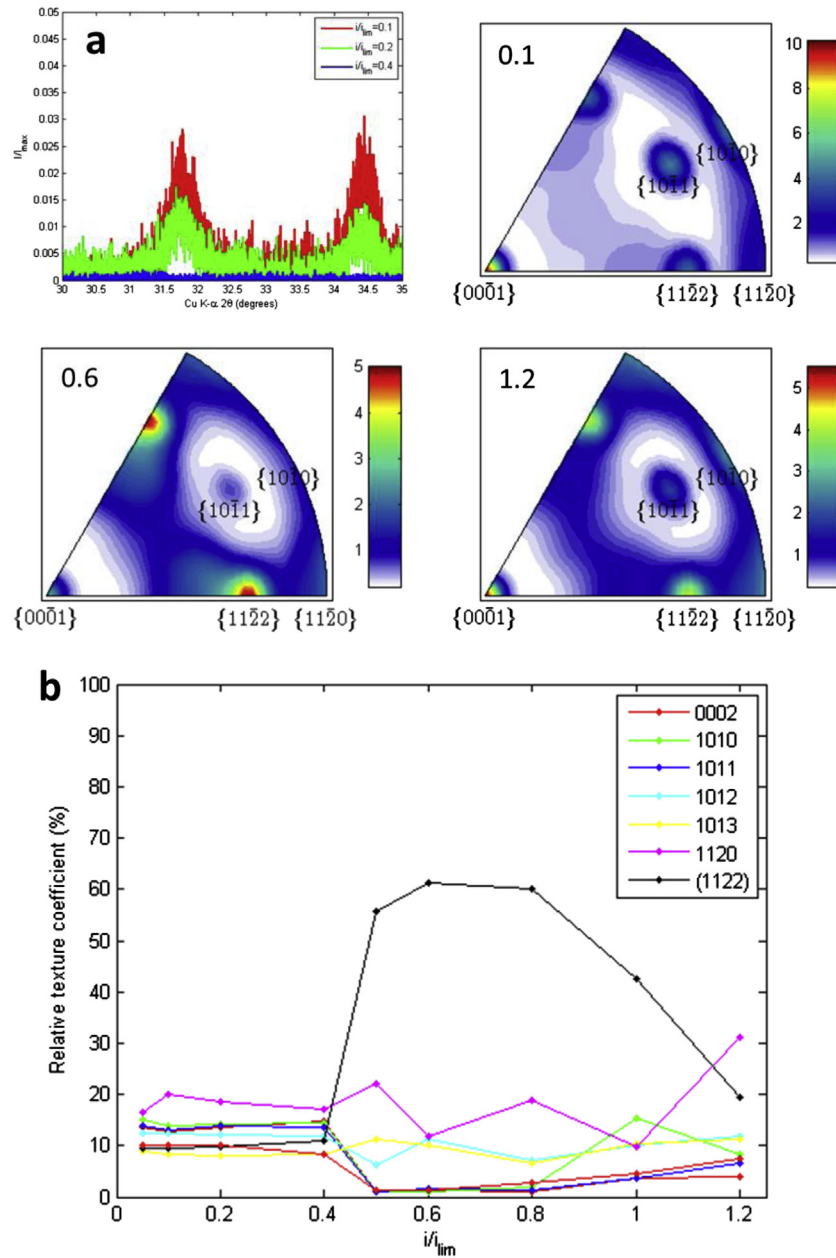
Fig. 4. (a) Inverse pole figures of zinc deposited at $i/i_{lim} = 0.1, 0.6$ and 1.2 ($i_{lim} = 50$ mA cm^{-2}). (b) Relative texture coefficients of the prominent zinc reflections are reported at each i/i_{lim}.

with a mix of $(11\bar{2}2)$, $(10\bar{1}0)$ and $(11\bar{2}0)$ being the dominant reflections.

We explain our results using Pangarov's theory of preferred orientation of electrodeposited metals [4,24]. The work function of

zinc deposition is postulated to vary depending on the orientation. According to this, the nucleation rate of a given orientation is given by equation (4):

$$I_{st} \propto \exp\left(-\frac{W_{hkil}}{kT}\right) \tag{4}$$

It is clear from the above that the nucleation rate at a given overpotential is highest for the orientation with the lowest work function (W_{hkil}). If W_{hkil} of a given orientation is significantly lower than others, it would be preferred, and probably form a deposit with significantly fewer grain boundaries. The work function itself is related to the overpotential by equation (5):

$$W_{hkil} = \frac{B_{hkil}}{Fz\eta - A_{hkil}} \tag{5}$$

where A_{hkil} and B_{hkil} are constants that account for the work of removing a single atom from a half-crystal position and a crystal

Table 1
Texture coefficient of zinc deposits calculated from XRD data.

i (mA cm^{-2})	i/i_{lim}	TC(00$\bar{0}$2)	TC(10$\bar{1}$0)	TC(10$\bar{1}$1)	TC(11$\bar{2}$0)	TC(11$\bar{2}$2)
2.5	0.05	1.053	1.153	1.062	1.277	0.744
5	0.1	1.015	1.110	1.049	1.599	0.763
10	0.2	1.145	1.093	1.073	1.437	0.769
20	0.4	1.051	1.116	1.047	1.315	0.854
25	0.5	0.139	0.144	0.149	2.951	7.411
30	0.6	0.157	0.127	0.203	1.495	7.702
40	0.8	0.145	0.264	0.186	2.453	7.872
50	1	0.406	1.660	0.414	1.061	4.643
60	1.2	0.424	0.903	0.711	3.342	2.098

edge respectively. The development of preferred orientation on zinc is understood from the overpotential dependence of work function. At low overpotentials, the work functions of nearly all orientations are high, and the nucleation rate is adversely affected. Although the $(000\bar{2})$ orientation should be favored, the choice of preferred direction is very sensitive to fluctuations in overpotential, which occur due to the non-linear nature of the Butler–Volmer equation. This leads to a mixture of orientations, the ensemble average of which closely resembles finely powdered zinc.

The modified Butler–Volmer equation is most insensitive overpotential fluctuations at intermediate values. It is for this reason the overpotential-dependent preferred growth orientation remains unperturbed by moderate fluctuations in the current density at intermediate values of $i/i_{\lim}$. Although Pangarov predicts the $(10\bar{1}0)$ orientation to dominate at intermediate overpotentials, we report the $(11\bar{2}2)$ direction to dominate on brass. This discrepancy is not unexpected, since a substrate effect is expected to be present, and the $(10\bar{1}0)$ oriented growth is valid for an inert substrate that does not affect the values of A_{hkil} and B_{hkil}. The choice of substrate [25,26] could potentially be another innovation to optimize the work function to improve the selectivity of a given orientation, ensuring finer deposits. Predicting preferred orientation at $i/i_{\lim} \sim 1$ is complex on account of the large changes in overpotential associated with hydrogen co-evolution. Although $(11\bar{2}2)$ is predicted to be the dominant form, we observe a mix of $(10\bar{1}0)$, $(11\bar{2}0)$ and $(11\bar{2}2)$. The potential fluctuates widely, and the final deposit is dominated by a mix of two or more orientations. Potentiostatic zinc deposition experiments are needed to compute the values of A_{hkil} and B_{hkil} and further clarify the selection of preferred growth direction.

3.3. Impedance behavior of zinc electrodeposits

Although it is clear that compact zinc has the best performance, the governing processes need to be formulated within a mathematical framework. Potentiostatic EIS experiments were performed on a copper RDE to investigate the frequency dependence of charge-transfer, ohmic and mass-transfer processes at the electrode. The rotation speed was varied between 100 and 2500 rpm to obtain an insight into the effect of convection on the reaction kinetics.

The representative behavior at different potentials is shown in a Bode plot (Fig. 5a). The asymptotic high frequency impedance across all the experiments is 0.5 Ω cm^2, indicating that the ionic conductivity of the electrolyte (400 mS cm^{-1}) [27] is almost completely unaffected for the range of overpotentials reported.

Prior to electrode activation ($E = -1410$ mV), the low frequency impedance rises sharply due to surface blockage by a solid ZnO film. The current density during electrode activation ($E = -1440$ mV) is $\sim$10 mA cm^{-2} and is the lower limit for the formation of compact zinc. The thickness of the ZnO film rapidly drops after activation (-1490 mV $< E < -1440$ mV) and charge-transfer and zincate depletion in the boundary layer make comparable contributions to the impedance. At $E < -1540$ mV, the low frequency impedance rises sharply on account of zincate depletion from the boundary layer.

The impedance is corrected for the ohmic drop and scaled by the charge-transfer resistance (R_{ct}), shown in a Nyquist plot (Fig. 5b). At $E = -1410$ mV, the straight line at 45° indicates an infinite Warburg impedance due to the impervious ZnO film described previously. The absence of a high frequency capacitive (HFC) implies that the ZnO layer hinders the charge-transfer step. Zinc is deposited only at the pores in the ZnO film, which explains the porous structure. The efficiency of the charge-transfer process improves at higher potentials due to the thinning/increased porosity of the ZnO film. The Nyquist plot of an activated electrode comprises a high frequency capacitive (HFC) loop due to the relaxation of the electrical double layer, a low frequency inductive (LFI) loop due to the formation of an absorbed intermediate, and a low frequency capacitive (LFC) due to the zincate depletion in the boundary layer. The adsorbed intermediate is consumed at higher potentials and the LFI loop diminishes in size and disappears completely at $E = -1540$ mV. The mass-transfer contribution (LFC) in the boundary layer is represented by a finite Warburg element. The LFC response is always slower than the LFI, meaning that the zincate in the boundary layer is depleted only after the intermediate is consumed. The LFC loop increases with applied overpotential, and the thickness of the boundary layer increases until it is essentially infinite. This is represented by the 45° line appearing after the charge-transfer loop for $E = -1580$ mV.

We explain our results by assuming the deposition kinetics to be given by a Butler–Volmer expression modified by the limiting current density. The current density is given by equation (6):

$$i = i_0 \left[\exp(\alpha_c f \eta) - \left(1 - \frac{i}{i_{\lim}} \right) \exp(-\alpha_a f \eta) \right] \quad (6)$$

where $f = nF/RT$, i_0 is the exchange current density (mA cm^{-2}), $-1/\alpha_a f$ and $1/\alpha_c f$ are the anodic and cathodic Tafel slopes respectively. The steady-state potentiostatic current was determined at 100, 400 and 2500 rpm and is given in Fig. 6. Increasing the rotation speed increases the anodic current by increasing the
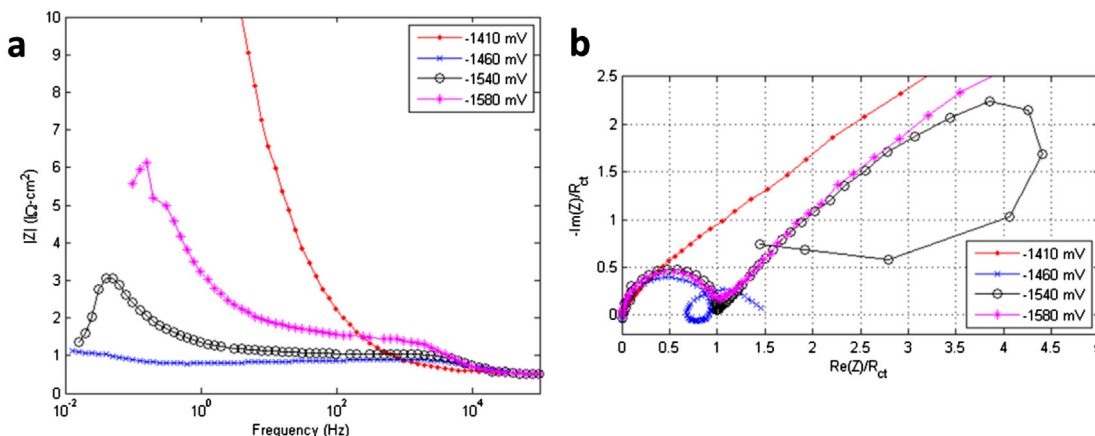

Fig. 5. (a) Bode and (b) Nyquist plots at 100 rpm to isolate the timescales of the kinetic, ohmic and mass-transfer processes in zinc deposition.

mass-transfer limiting current and lowering the concentration overpotential. The limiting current densities at 100, 400 and 2500 rpm are -81, -151 and -375 mA cm^{-2} respectively. The ohmic contribution to the overpotential is subtracted and the experimental data was fitted using equation (6) to obtain i_0 and α_a. The experimental data is well fit by the above expression and the values of the kinetic parameters are summarized in Table 2. The exchange current density is in good agreement with reported literature for zinc deposition in alkaline electrolyte ($i_0 = 0.21$ mA cm^{-2}) [28]. The values of i_0, α_a and α_c remain almost constant even after the rotation speed is changed by a factor of 25, indicating our analysis of the $E-i$ data to be accurate.

Differentiating expression for the current density typically yields the charge-transfer resistance. However, our expression for the current accounts for the diffusive contribution (R_D), we obtain the total cell resistance instead as:

$$R_{tot} = R_{ct} + R_D = \left[\frac{\partial \eta}{\partial i}\right]_{C_{Zn}, C_{OH}} \tag{7}$$

to obtain equation (8):

$$R_{tot} = \frac{\left[\frac{1}{i_0} - \frac{\exp(-\alpha_a f \eta)}{i_{lim}}\right]^2}{\frac{f}{i_0}[\alpha_c \exp(\alpha_c f \eta) + \alpha_a \exp(-\alpha_a f \eta)] - \frac{(\alpha_c + \alpha_a)}{i_{lim}}\exp[(\alpha_c + \alpha_a)f\eta]} \tag{8}$$

The value of R_{tot} approaches infinity at OCV and at the limiting current, and must be minimum at some intermediate value. We elaborate on our earlier premise that compact zinc deposition corresponds to the minimum overall resistance [13]. The ratio (i/i_{lim}) corresponding to this minimum, obtained is differentiating the expression for R_{tot}:

$$\frac{\partial R_{tot}}{\partial i} = R_{tot}^3 \left(\frac{\partial^2 i}{\partial \eta^2}\right) = 0 \tag{9}$$

to yield equation (10), the condition for the minimum R_{tot}.

$$\frac{i}{i_{lim}} = 1 - \frac{\exp(\alpha_c f \eta)\left[\frac{\alpha_c^2}{i_0} - \frac{2\alpha_c \alpha_a + \alpha_c^2}{i_{lim}}\exp(-\alpha_a f \eta)\right]}{\alpha_a^2 \left[\frac{\exp(-\alpha_a f \eta)}{i_0} + \frac{\exp(-2\alpha_a f \eta)}{i_{lim}}\right]} \tag{10}$$

Table 2
Kinetic parameters evaluated from $E-i$ data.

Parameter	100 rpm	400 rpm	2500 rpm
i_0 (mA cm^{-2})	0.2	0.2	0.2
i_{lim} (mA cm^{-2})	-81	-151	-375
α_c	0.65	0.67	0.69
α_a	0.35	0.33	0.31

Equation (10) is solved to obtain the overpotential η_{min} corresponding to the minimum value of R_{tot}, which is substituted in equation (9) to determine R_{tot}. The value of i/i_{lim} that satisfies equation (10) is insensitive to η_{min} and is typically $i/i_{lim} \sim 0.5$. The EIS data was fitted to an equivalent circuit model [28] and the values of R_{ct} and R_D were determined by fitting the EIS data (Fig. 6b). The theoretical value of R_{tot} was then compared with the experimentally determined value. It is observed that both plots have a minimum resistance of 0.59 Ω cm^2 at an ohmically-corrected $\eta = -60$ mV, which corresponds to $i/i_{lim} = 0.5$. The values of R_{ct} and R_D have their own minima which do not overlap and there is good agreement between the theory and experiment. The actual R_{tot} rises sharply on either side of the minimum, increasing by nearly an order of magnitude for $i/i_{lim} = 0.1$ or $i/i_{lim} = 1$. This result lends credibility to the use of i/i_{lim} as a characterization metric and establishes that optimal zinc electrode performance is obtained when $i/i_{lim} = 0.5$.

3.4. Effect of morphology on electrode performance

Zinc was deposited galvanostatically at different current densities on a rotating disk electrode at 50 rpm ($i_{lim} = -55$ mA cm^{-2}) and 200 rpm ($i_{lim} = -110$ mA cm^{-2}), followed by slow galvanostatic dissolution at 5 mA cm^{-2} until the electrode potential rose to -1.25 V. Fig. 7a indicates that the current density ratio is a satisfactory metric to ascertain the performance of different zinc morphologies. The coulombic efficiencies of zinc deposited at different RDE speeds almost overlap each other, even though the rotation speed is increased by a factor of 4. At very low current densities, the coulombic efficiency drops off due to the effect of a ZnO layer that prevents efficient charge transfer (kinetic control). At high current densities ($i > i_{lim}$), the zincate concentration effectively drops to zero and hydrogen is evolved at the electrode instead (mass-transfer control). The coulombic efficiency for current densities in excess of the limiting current is nearly i_{lim}/i,
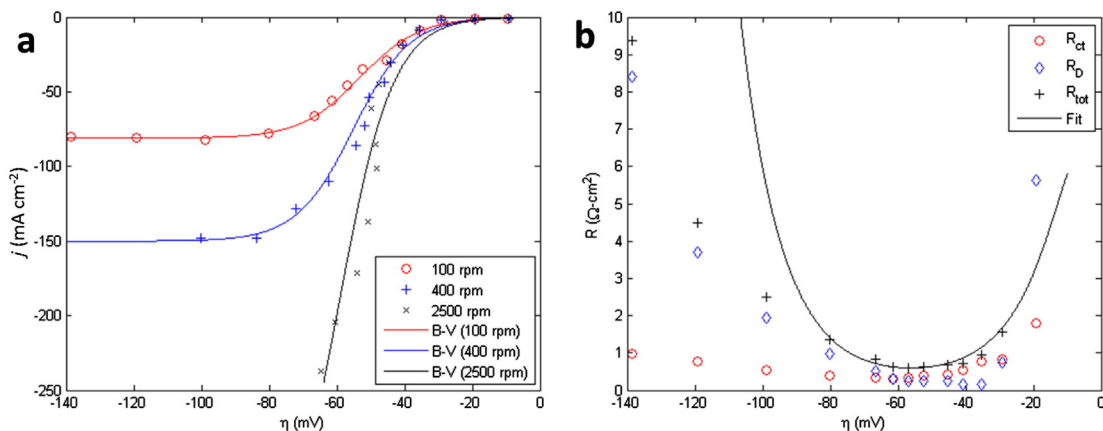
Fig. 6. (a) Polarization plots of zinc deposited at 100, 400, and 2500 rpm are fitted to a single value of i_0 and α_a. (b) Plot of total resistance R_{tot} obtained from equation (8) compared with experimental R_{tot} calculated from EIS data.
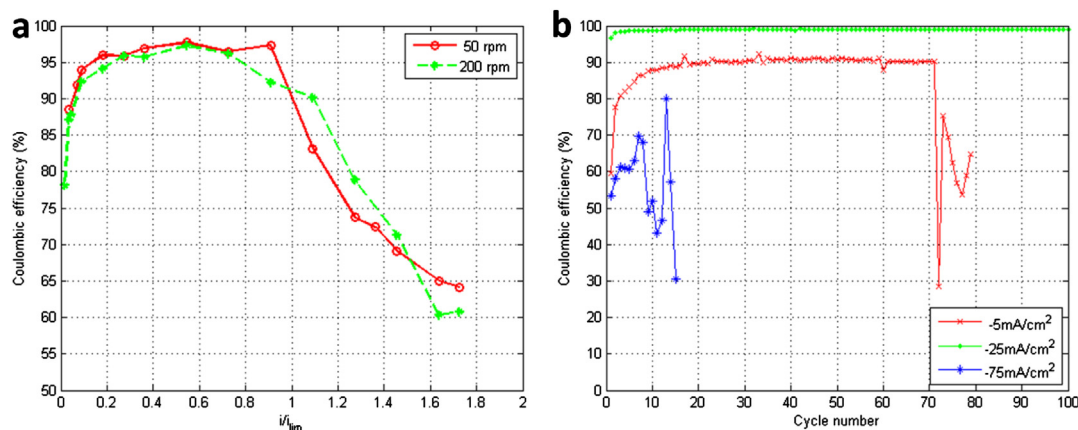
Fig. 7. (a) Coulombic and energy efficiency of zinc deposition in a single cycle and (b) effect of cycling on the coulombic efficiency of zinc deposition at $i = -5, -25$ and -75 mA cm^{-2}. The limiting current was $i_{lim} = -55$ mA cm^{-2}.

the fractional contribution of deposition current to zinc deposition.

Zinc was cycled using the same protocol as the galvanostatic experiments mentioned above to investigate the long-term effectiveness of different zinc morphologies. Compact zinc (-25 mA cm^{-2}) clearly has the best performance, with coulombic efficiencies excess of 99% over 100 cycles. The coulombic efficiency of mossy zinc improved to about 90% for up to 70 cycles. However, the inefficient charge transfer due to the ZnO formation and increasing impedance led to the failure of the anode on the 80th cycle. Dendritic zinc (-75 mA cm^{-2}) is accompanied with hydrogen bubbling and blocks zincate ions from reaching the electrode. The efficiency on succeeding cycles drops rapidly and the electrode is unable to accept any charge after the 16th cycle. The impressive performance of preferentially-oriented zinc morphologies merits some rethinking in battery charging strategies. Zinc anodes are typically used in stagnant systems, often coupled with cathodes that prefer a slower charge rate. Zinc anodes seem to work best at moderate charging current densities, which is contrary to charging protocols usually employed. The use of a slow battery charging protocol leads to zinc growing under kinetic control, and eventual failure due to the charge transfer resistance increasing with cycle number. However, high currents deplete zincate ions from the electrolyte boundary layer, which is a major problem in stagnant systems. The use of pulse charging has been previously used to produce conformal zinc deposits [29], and could be an innovation to remove kinetic and mass-transfer limitations associated with zinc-anode batteries.

4. Conclusion

Preferred orientation in compact zinc is shown to significantly improve performance and cycle life in flow-assisted alkaline zinc batteries. Compact zinc has the highest coulombic efficiency of 99% over 100 cycles. EIS and XRD experiments confirm the hypothesis that compact zinc occurs at a minimum of the overall cell resistance, and a $(11\bar{2}2)$ orientated texture is observed for compact zinc deposits on brass. Following Pangarov's theory, preferred orientation is related to the orientation with the minimum work function of nucleation. Mossy zinc is formed at $i/i_{lim} < 0.3$ due to the presence of a thin film of ZnO impeding charge transfer is confirmed. Although the timescales of the ohmic, kinetic and mass-transfer processes at the zinc electrode were determined, there is sufficient motivation for an EIS model of the zinc that accounts for the ZnO layer and zincate depletion. The morphological control of zinc deposits, by use of novel substrates or electrolyte additives [30] are interesting topics meriting further research.

References

[1] T. Adler, F. McLarnon, E. Cairns, J. Electrochem. Soc. 140 (1993).
[2] Y. Ito, M. Nyce, R. Plivelich, M. Klein, D. Steingart, S. Banerjee, J. Power Sources 196 (2011) 2340.
[3] J. Cheng, L. Zhang, Y.-S. Yang, Y.-H. Wen, G.-P. Cao, X.-D. Wang, Electrochem. Commun. 9 (2007) 2639.
[4] N. Pangarov, Electrochim. Acta 7 (1962) 139.
[5] K. Saber, C. Koch, P. Fedkiw, Mater. Sci. Eng. A 341 (2003) 174.
[6] A. Despic, M. Pavlovic, Electrochim. Acta (1982) 1539.
[7] J.O. Bockris, Z. Nagy, A. Damjanovic, J. Electrochem. Soc. 119 (1972) 285.
[8] M.V. Simicic, K.I. Popov, N.V. Krstajic, J. Electroanal. Chem. 484 (2000) 18–23.
[9] C. Cachet, B. Saidani, R. Wiart, Electrochim. Acta 33 (1988) 405–416.
[10] O. Devos, O. Aaboubi, J. Phys. Chem. B 103 (1999) 496–501.
[11] R. Naybour, Electrochim. Acta 13 (1968) 763–769.
[12] D. Grier, E. Ben-Jacob, R. Clarke, L. Sander, Phys. Rev. Lett. 56 (1986).
[13] Y. Ito, X. Wei, D. Desai, D. Steingart, S. Banerjee, J. Power Sources 211 (2012) 119.
[14] K. Popov, D. Keca, M. Andjelic, J. Appl. Electrochem. 9 (1978) 19.
[15] R. Aogaki, J. Electrochem. Soc. 129 (1982) 2447.
[16] J. Elezgaray, J. Electrochem. Soc. 145 (1998) 2016.
[17] J. Diggle, A. Despic, J. Bockris, J. Electrochem. Soc. 116 (1969).
[18] L. Berube, G. L'Esperance, J. Electrochem. Soc. 136 (1989) 2314.
[19] C. Madore, M. Matlosz, D. Landolt, J. Appl. Electrochem. 22 (1992) 1155.
[20] R. Hielscher, H. Schaeben, J. Appl. Crystallogr. 41 (2008) 1024.
[21] C. Cachet, J. Electrochem. Soc. 138 (1991) 678.
[22] C. Madore, D. Landolt, Plat. Surf. Finish. (August 1995) 37.
[23] J.W. Gallaway, D. Desai, A. Gaikwad, C. Corredor, S. Banerjee, D. Steingart, J. Electrochem. Soc. 157 (2010) A1279.
[24] N. Pangarov, J. Electroanal. Chem. 9 (1965) 70.
[25] M. Chu, J. McBreen, G. Adzic, J. Electrochem. Soc. 128 (1981) 2281.
[26] J. McBreen, M. Chu, G. Adzic, J. Electrochem. Soc. (1981) 2287.
[27] J. Newman, K.E. Thomas-Alyea, Electrochemical Systems, third ed., John Wiley & Sons, 2012.
[28] K. Youssef, C. Koch, P. Fedkiw, Corros. Sci. 46 (2004) 51.
[29] A. Despic, K. Popov, J. Appl. Electrochem. 1 (1971) 275.
[30] J.W. Gallaway, A.M. Gaikwad, B. Hertzberg, C.K. Erdonmez, Y.-C.K. Chen-Wiegart, L.A. Sviridov, K. Evans-Lutterodt, J. Wang, S. Banerjee, D.A. Steingart, J. Electrochem. Soc. 161 (2013) A275.